Advances in
Geo-Energy Research

Vol. 14, No. 3, p. 170-186, 2024

Original article

Effects of pore pressure on coring-induced damage based on simulation by mesoscale stress-flow coupling numerical model

Leilei Zhao[1,2,3], Ruidong Peng[1,3]*, Pengfei Hao[1,3], Yu Yang[1,3], Hongwei Zhou[1]

[1] *State Key Laboratory for Fine Exploration and Intelligent Development of Coal Resources, China University of Mining and Technology (Beijing), Beijing 100083, P. R. China*

[2] *Key Laboratory of Xinjiang Coal Resources Green Mining, Ministry of Education, Xinjiang Institute of Engineering, Urumqi 830023, P. R. China*

[3] *School of Mechanics and Civil Engineering, China University of Mining and Technology (Beijing), Beijing 100083, P. R. China*

Keywords:
Deep rock mechanics
in-situ pressure-preserved coring
pore pressure
elastic-plastic-damage model
stress-flow coupling

Cited as:
Zhao, L., Peng, R., Hao, P., Yang, Y., Zhou, H. Effects of pore pressure on coring-induced damage based on simulation by mesoscale stress-flow coupling numerical model. Advances in Geo-Energy Research, 2024, 14(3): 170-186.
https://doi.org/10.46690/ager.2024.12.03

Abstract:
The deep *in-situ* environment is often characterized by high pore pressure, which will be released during traditional coring in deep rocks and lead to damage in rock samples. Hence, a novel coring technology has been proposed and systematically investigated for preserving *in-situ* conditions, including pore pressure, to obtain rock samples with high fidelity to the deep *in-situ* environment. To theoretically examine the variation in pore pressure after coring and evaluate its influence on rock samples, two kinds of mesoscopic model representing closed-pore and open-pore were established and analyzed by stress-flow coupling, in which both seepage in porous matrix and flow in relatively bigger cavities are considered. An elastic-plastic-damage model associated with volumetric dilatation was introduced to reflect tensile damage. The influences of pore pressure after different kinds of coring were simulated by a series of conceptualized models, and the results revealed three kinds of situations: Pore pressure removal, pore pressure release, and pore pressure preservation. During traditional coring, the high pore pressure will neither be sealed completely nor released suddenly because the rock matrix has low permeability. The higher residual permeation pressure in the rock matrix will be caused by lower permeability, larger closed cavities or smaller open cavities. During traditional coring, the coring-induced inner damage arises nearby closed cavities. Both the damage value and the damage zone are increased with decreasing permeability. However, extra tensile damages rarely arise during *in-situ* pore pressure-preserved coring, which technology can also retain *in-situ* high pressure. Hence, the *in-situ* pore pressure-preserved coring technology has great significance for eliminating the distortion effect of coring to the greatest possible extent.

---

1. Introduction

Deep energy exploitation is of increasing interest because of the gradual depletion of shallow resources, such as minerals, coal, hydrocarbon, geothermal, et al. (Xie et al., 2021a) Many projects have reached new heights in terms of drilling depth. For example, the Barnett shale completion reaches a depth of 2,500 m (Tang et al., 2016). The exploitation depth of Shunbei oil and gas field in the Tarim Basin is 7,200-8,800 m (Ma et al., 2022). However, the deep *in-situ* environment characterized by high ground stress, high temperature, high permeation pressure and strong engineering disturbances leads directly to the change of rock mechanical properties and a high frequency of engineering accidents (Cao et al., 2022). Many

---

Yandy Scientific Press

*Corresponding author.

E-mail address: zhaolei198704@163.com (L. Zhao); prd@cumtb.edu.cn (R. Peng); hpf804489212@gmail.com (P. Hao); yangyu201809@163.com (Y. Yang); zhw@cumtb.edu.cn (H. Zhou).

Received September 3, 2024; revised October 1, 2024; accepted October 20, 2024; available online October 26, 2024.

studies have been carried out regarding the characteristics of deep rocks, such as the nonlinear evolution law with depth (Xie et al., 2020), long-term mechanical characteristics (Zha et al., 2021), dynamic features (Zhao et al., 2020), the temperature effect (Liu et al., 2020), the liquid absorption effect (Shen et al., 2018), fracture behaviors under different loading conditions (Hokka et al., 2016) and so on. These studies have promoted the understanding and development of deep rock mechanics.

However, most of these researches depend on rock samples obtained by traditional coring technologies, which are exposed directly to the atmosphere such that the initial state of rocks has been disturbed and the *in-situ* information is lost. Therefore, traditional coring samples cannot reflect the true physical and mechanical properties of rock in the *in-situ* environment, such as elastic modulus, Poisson's ratio, density, etc. Some new coring technologies are ongoing and mainly focus on thermal insulation and *in-situ* pressure preservation (Zhu et al., 2013). The team of academician Heping Xie has done a great deal of research on this scientific challenge in recent years and proposed a novel coring technology for preserving the *in-situ* conditions, including pore pressure, temperature, quality, luminosity, and humidity (Xie et al., 2021b).

As a matter of fact, pore pressure plays an important role in rock failure and engineering stability (Di et al., 2022). For example, high pore pressure leads to various gas disasters and accidents in the process of coal mining (Gao et al., 2021). The leakage of pore pressure in excavation often occurs and threatens engineering safety (Chen et al., 2017). Pore pressure also plays a significant role in well design in oil and gas exploitation, seriously affecting wellbore stability, and potentially causes kicking, blowout and other complications, leading to drilling accidents. The reason is that rock material is a porous medium, which contains various defects such as fissures, voids and joints, providing spaces for multiphase fluids (Golparvar et al., 2018). The pore pressure inside rock material will result in significant differences in the internal structure and physical properties of rock. Zhang et al. (2021) researched the pore pressure effect and sensitivity of bituminous coal deformation. Zhou et al. (2022) tested the creep characteristics of red sandstone under the conditions of high temperature and confining pressure at different pore pressures. Nonetheless, further research on pore pressure is still needed because of the lack of comprehensive testing instruments and experimental methods.

In terms of rock samples, cores taken from the *in-situ* environment simultaneously undergo stress unloading and pore pressure releasing effects. In addition to the stress unloading effect, pore pressure release will also change the internal stress state and meso-structure of rock samples because the fluids inside rock pore will seep out. For instance, Du et al. (2019) observed the significant deformation and failure phenomenon of coal samples by the adsorption-instantaneous pressure relief test. The damage and even fracture emerged when the gas pressure released instantaneously. It could be inferred that the greater the pore pressure in the *in-situ* deep environment, the greater the damage caused by pore pressure release in the process of drilling coring. Therefore, the initial damage of cores is caused by the sudden release of geostress and pore pressure during coring. Some discing in rock cores might arise during coring especially in the high geostress zone (Xie et al., 2020). This phenomenon can be attributed to the damage caused by coring. Furthermore, ordinary samples are always placed in geostress and pore pressure recovery devices to consider the *in-situ* conditions. Thus, the rock samples will undergo stress reloading and pore pressurization, which will inevitably cause secondary damage or destruction. Hence, the samples obtained by traditional coring technologies cannot reflect the true state and characteristics of the deep *in-situ* environment, and even lead to errors in the laboratory test results. At present, some scholars have begun to study the damaging effect of geostress release on rock caused by coring (Yan et al., 2016). However, the damaging effect of pore pressure release on rock during coring has never been studied.

Therefore, it is necessary to investigate the mechanisms and effects of pore pressure release during the coring process to discuss the importance of pore pressure preservation. In traditional rock mechanics, rock samples are often treated as a porous elastic media by means of phenomenological methods (Chao et al., 2021). However, this approach fails to reflect the fluid flow behaviors in actual rock pores and fissures. Hence, the releasing process of pore pressure during coring should be examined from a mesoscopic perspective involving solid deformation, fluid flow and seepage. Meanwhile, field monitoring and laboratory experiments are difficult to be implemented at mesoscopic scales in the current technological environment. Fortunately, several numerical simulation studies about rock damage, fluid flow and seepage were executed (Zhou et al., 2018; La Spina et al., 2020; Wu et al., 2024). The achievements made by these works provide a possibility for the research of the damage effect caused by pore pressure releasing during coring. Nonetheless, some reasonable representative models need to be further established under stress-flow fields coupling and then realized by numerical simulation.

The remainder of this paper is organized as follows: The theoretical basis and governing equations are presented in Section 2; the numerical simulation scheme is described in Section 3; the results are illustrated and discussed in Section 4; the conclusions are finally drawn in Section 5.

2. General assumptions and governing equations

2.1 General assumptions

Thus far, a significant number of studies have indicated that there are plenty of voids, fractures, nanopores, and circulation channels in rock materials at the mesoscopic scale (Zhang et al., 2023). Zhao et al. (2022) compared the microstructure of rock samples with or without pore pressure. The comparative results showed that the number and range of pores increases significantly due to the effect of pore pressure (Fig. 1).

Based on the above, rocks can be considered as non-continuum media containing a large number of open and closed pores with different morphologies. The closed-pore structure (indicated by green dash circles) resembles a closed cavity, which is surrounded by rock matrix, and provides

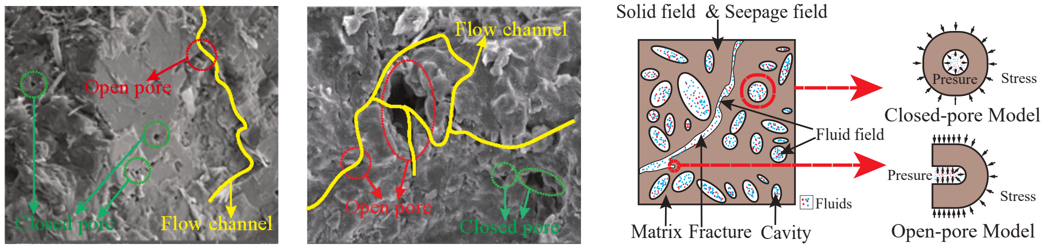

(a) (b) (c)

Fig. 1. SEM image and schematic diagram of rock structure. (a) SEM image without pore pressure, (b) SEM image with pore pressure and (c) schematic diagram.

storage space for fluids. Meanwhile, open-pore structures (indicated by red dash circles) are connected by some peripheral fissures or cracks, forming a flow channel (indicated by yellow curve lines) for fluids. The fluids stored in the open pores can flow freely into other cracks, while the fluids stored in the closed pores can be sealed by the surrounding solid matrix. When rocks are deformed, some closed pores might evolve to be open pores due to the damage and fracture of the rock matrix, while some open pores might be sealed to become closed pores due to the movement and contact of opposite pore walls. Besides, the rock matrix still contains various nanopores that are invisible at the mescoscale, which can form extremely small-sized crack networks for the permeation and diffusion of fluids in the rock matrix. Hence, the rock matrix should not be denoted as a simple impermeable solid phase but considered as a tight porous medium in which seepage occurs at a relative smaller scale. Accordingly, two kinds of representative models at the mesoscopic scale, as shown in Fig. 1(c), namely, a closed-pore model and an open-pore model, will be built and simulated.

Firstly, as mentioned above, several assumptions were proposed in this paper:

1) The rock materials are composed of porous solid matrix and relative larger cavities. These cavities are separately grouped into closed cavities or open cavities. The porous solid matrix is considered as a medium that is an elastic-plastic-damage continuum. The cavities are relative larger pores, while the pores in matrix are more smaller.
2) Both the porous matrix and cavity contain a fluid phase. Fluid flow in the closed or open cavities is treated as laminar flow. Because of the abundance of smaller holes and fissures, fluid flow in the porous matrix is described as seepage by Darcy's law.
3) The pore pressure is usually high in the deep *in-situ* environment, and the fluid density is sensitive to high pressure (Liu et al., 2017). Thus, rather than incompressible fluid, compressible fluid was adopted in the simulation.

2.2 Theoretical basis and governing equations

2.2.1 Pore pressure effect

In numerical simulations, the effect of pore pressure can be treated as no influence, additive stress, effective stress or residual stress. These four scenarios are compared and their differences are summarized in Table S1 in the supplementary file. In this study, both displacement boundary and pressure boundary will be adopted. Hence, an additive stress can best represent the effect of pore pressure. It's described as:

$$\sigma = \mathbf{C} : (\varepsilon - \varepsilon_{\mathbf{ie}}) + \alpha_B P \mathbf{I} \tag{1}$$

where σ denotes stresses of solid structure, Pa; ε denotes total strains; ε_{ie} refers to the inelastic strains; $\mathbf{C}$ represents the fourth order elasticity tensor, Pa; P denotes pore pressure, Pa; $\mathbf{I}$ is the identity tensor; α_B denotes the Biot's coefficient, whose value can be set as 0.3 for most rocks (Zhu et al., 2011). This means that the compressive stresses are augmented due to the existence of pore pressure. The pore pressure and compression stress are both expressed as positive values in this paper.

The additive stress obtained by adding pore pressure presents larger stress that could impact the plastic deformation and damage of the solid matrix; it can overcome the limitation of effective stress in which pore pressure is eliminated from the stress tensor. Moreover, the effect of pore pressure on various boundaries is also considered, which compensates the shortage of residual stress where pore pressure has no influence on deformation.

2.2.2 Elastic-plastic damage model

In the process of rock deformation and failure, damage will arise inevitably. Numerous damage models have been built to describe the rock failure behavior (Li et al., 2012; Bruning et al., 2019; Zhang et al., 2022) based on rock damage mechanics. Following these works, an elastic-plastic-damage model is proposed in this section.

The direct damage effect is commonly characterized by degrading the elasticity modulus of rock materials, which can be represented by:

$$\mathbf{C} = \mathbf{C}_0 (1 - D) \tag{2}$$

where D denotes the damage variable; $\mathbf{C}_0$ is the initial elasticity tensor, Pa.

According to many studies, the exponential function agrees well with the law of rock damage evolution. In this paper, the damage is supposed to be associated with the volume expansion, thus the damage variable is defined by:

$$D = 1 - \exp\left(-a\varepsilon_v^t\right) \tag{3}$$

where ε_v^t represents the volumetric strain of expansion expressed as a positive value; a is the dimensionless coefficient.

In addition, the Drucker-Prager plastic yield function combined with plastic hardening function and the damage variable is represented:

$$f = \alpha \mathbf{I_1} - \sqrt{\mathbf{J_2}} + (1-D)\,hR \tag{4}$$

where $\mathbf{I_1}$ represents the first invariant of the nominal stress tensor, Pa; $\mathbf{J_2}$ represents the second invariant of the nominal deviatoric stress tensor, Pa^2; α and R (Pa) represent the Drucker-Prager parameters; h is the plastic hardening function. The associated flow rule f is adopted for simplification.

Under the condition of matching the outer corner circumscribed circle of the hexagon of Mohr-Coulomb criterion, the Drucker-Prager parameters α, R can be represented by:

$$\begin{aligned} \alpha &= \frac{2\sin\varphi}{\sqrt{3\,(3-\sin\varphi)}} \\ R &= \frac{2\sqrt{3}c\cos\varphi}{3-\sin\varphi} \end{aligned} \tag{5}$$

where c denotes the cohesion of rock, Pa; φ denotes the internal frictional angle of rock (°).

The plastic hardening function (Zhang et al., 2016) is expressed by:

$$h = h_0 + (h_1 - h_0)\,\frac{\gamma^p}{b+\gamma^p} \tag{6}$$

where h_0 and h_1 are coefficients that represent the initial yield strength and the ultimate yield stress, respectively; b reflects the plastic hardening rate; γ^p is the effective plastic strain expressed as:

$$\gamma^p = \frac{\sqrt{2}}{3}\sqrt{\left(\varepsilon_1^p - \varepsilon_2^p\right)^2 + \left(\varepsilon_2^p - \varepsilon_3^p\right)^2 + \left(\varepsilon_1^p - \varepsilon_3^p\right)^2} \tag{7}$$

where ε_1^p, ε_2^p, ε_3^p are plastic strains in the three principal stress directions.

2.2.3 Seepage field

The transfer of gas or liquid in porous media is governed by Darcy's law (Yang et al., 2016), and the seepage equation can be described by Eq. (8):

$$\begin{gathered} \frac{\partial}{\partial t}\left(\rho_f \omega\right) + \nabla\cdot\left(\rho_f \mathbf{V_D}\right) = Q_m \\ \mathbf{V_D} = \frac{\kappa}{\mu}\nabla P \end{gathered} \tag{8}$$

where ρ_f denotes fluid density, kg/m^3; ω denotes matrix porosity; $\mathbf{V_D}$ denotes Darcy's velocity, m/s; κ denotes matrix permeability, m^2; μ denotes the dynamic viscosity of fluid, Pa·s; Q_m is source item, kg/(m^3·s).

The expression of storage model (Zhou et al., 2018) is represented by:

$$\frac{\partial}{\partial t}\left(\rho_f \omega\right) = \rho_f S_r \frac{\partial P}{\partial t} \tag{9}$$

where S_r denotes the storage coefficient shown as:

$$S_r = \omega c_r + \frac{(\alpha_B - \omega)(1-\alpha_B)}{K} \tag{10}$$

where c_r denotes the fluid compressibility coefficient, 1/Pa; K is the bulk modulus of the matrix, Pa.

When coupling the seepage field with the solid field, the source item (Zhou et al., 2018) in the seepage field can be expressed by:

$$Q_m = \rho_f \alpha_B \frac{\partial \varepsilon_v}{\partial t} \tag{11}$$

where ε_v represents the volumetric strain of matrix calculated in the solid mechanics field, with a positive value indicating volume compression.

The dynamic porosity and permeability (Yang et al., 2016) were deduced as:

$$\omega = \frac{V_{p0} - \Delta V}{V_0 - \Delta V} - \frac{\omega_0 - \varepsilon_v}{1 - \varepsilon_v} \tag{12}$$

$$\kappa = \kappa_0\left(\frac{\omega}{\omega_0}\right)^3 \tag{13}$$

where V_P denotes void volume in the matrix, m^3; V_{p0} denotes initial void volume, m^3; V_0 represents initial matrix volume, m^3; ΔV is the variation of matrix volume, m^3; ω_0 stands for the initial porosity of matrix; κ_0 is the initial permeability of matrix, m^2.

After combining Eqs. (8)-(13), the governing equation of the seepage field is shown as:

$$\begin{aligned} &\rho_f\left(\omega c_r + \frac{(\alpha_B - \omega)(1-\alpha_B)}{K}\right)\frac{\partial P}{\partial t} + \nabla\cdot\left[\rho_f\left(-\frac{\kappa}{\mu}\nabla P\right)\right] \\ &= \rho_f \alpha_B \frac{\partial \varepsilon_v}{\partial t} \end{aligned} \tag{14}$$

2.2.4 Fluid flow field

As mentioned above, the cavities provide storage space for free fluids, the flow of which obeys laminar flow with the pressure decreasing. The governing equations of laminar flow field include the Navier-Stokes equations describing conservation of momentum and the continuity equation describing conservation of mass (La Spina et al., 2020; Li et al., 2022). For compressible flow, the equations are expressed by:

$$\begin{aligned} &\rho_f \frac{\partial \mathbf{v}_L}{\partial t} + \rho_f \mathbf{V}_L\cdot\nabla\mathbf{V}_L = -\nabla P_L \\ &+ \nabla\cdot\left[\mu\left(\nabla\mathbf{V}_L + (\nabla\mathbf{V}_L)^T\right) - \frac{2}{3}\mu\left(\nabla\cdot\mathbf{V}_L\right)\mathbf{I}\right] + \mathbf{F}_V \end{aligned} \tag{15}$$

$$\frac{\partial \rho_f}{\partial t} + \nabla\cdot\left(\rho_f \mathbf{V}_L\right) = 0 \tag{16}$$

where $\mathbf{v}_L$ represents laminar flow velocity, m/s; P_L denotes the fluid pressure in fluid flow field, Pa.

2.2.5 Multi-field coupling method

In this paper, a closed-pore model and an open-pore model were separately built at the mesoscopic scale. The models involve three physical fields. The solid mechanical field and Darcy's seepage field were applied to the matrix simultaneous-

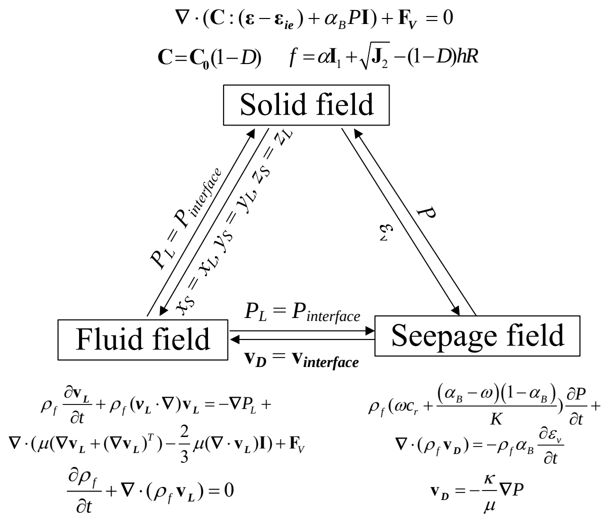

Fig. 2. Coupling relationship between the three physical fields.

ly, and the fluid flow field was applied to the cavity.

The fluid pressure P in Darcy's seepage field in the matrix could be treated as an external additive stress in the solid mechanical field. In turn, the volume strain rate of solid provided a source item for the seepage field. Besides, the volumetric strain of the solid matrix affected the matrix porosity and further influenced the permeability in Darcy's equation because of the cubic relationship between porosity and permeability.

The solid mechanics field and fluid flow field were applied to the matrix and the cavity, respectively. Therefore, the coupling of the two fields was implemented through interface parameters. The coupling effect of the solid mechanical field on the fluid flow field was realized by continuous coordinate values at the interface ($x_s = x_L$, $y_s = y_L$, $z_s = z_L$), where x_s, y_s, z_s were coordinate values in the solid mechanical field, and x_L, y_L, z_L were coordinate values in the fluid flow field. The fluid pressure at the interface calculated in the fluid flow field was applied as a surface load in the solid mechanical field ($P_L = P$). Similarly, the coupling effect of matrix seepage field and cavity flow field also occurred at the interface. The laminar flow velocity at the interface in the fluid flow field was adopted as Darcy's velocity to ensure that the speed values were continuous ($\mathbf{v}_L = \mathbf{v}_D$). The fluid pressure in the matrix seepage field was treated as the value calculated in the cavity flow field to realize continuous pressures at the interface ($P_L = P$). The coupling relationship between the three physical fields were shown in Fig. 2.

3. Numerical simulation scheme

A numerical model of 1/8 sphere was established by the 3D-FEM (finite element method) software COMSOL Multiphysics, which has various extension interfaces for users to modify the computational item and realize the convenient coupling of the above multi-fields. A 1/8 sphere with 500 μm radius was set up and another 1/8 sphere with 100 μm radius was built to denote the cavity, and the final geometric model was obtained by subtracting the two zones. The solid mechanics field and Darcy's seepage field were applied to the matrix zone to simulate the solid deformation and fluid seepage. The laminar flow field was applied to the cavity zone to simulate the free flow of fluid. In the model, a survey line and three monitoring points were arranged. The schematic diagram of numerical model is presented in Fig. 3.

It can be seen from Fig. 3 that a 1/8 numerical model was finally established to represent both the closed-pore and the open-pore model. Hence, the two models were realized merely by imposing different boundary conditions, which could be divided into internal boundary, pore wall surface, spherical outer surface, and outlet boundary, as shown in Fig. 3. In the closed-pore model, the internal boundaries were set to be symmetry planes in three fields. The spherical outer surface was set to be a displacement boundary used for stress loading and unloading in the solid mechanical field and an outlet boundary used for pore pressure released in the seepage field. The pore wall surface in the solid field and the seepage field were set to be the pressure boundary applied by the fluid pressure calculated in the fluid field. The pore wall surface in the fluid field was set to be the velocity boundary applied by seepage velocity, and the coordinates of the position were set to be equal to the values in the solid mechanical field.

In the open-pore model, the internal boundaries and wall surface were set to be same as in the closed-pore model. The spherical outer surface in the solid mechanical field was also set to be the same as the closed-pore model. The differences are that the spherical outer surface was set to be a symmetry boundary in the seepage field and the outlet boundary in the fluid field was set on an internal surface of cavity, which is perpendicular to the open direction of cavity, to simulate the pressure loading and unloading process.

In the numerical simulation, a stationary computing was first executed to simulate the *in-situ* scenario. Then, time-dependent computing was performed to simulate the coring process with stress unloading and pore pressure releasing effect. The spherical outer surface and outlet boundary were applied as constants in the stationary computing process and linearly decreasing in the time-dependent computing process. To reflect the stress unloading and the rapid release of pore pressure in the process of coring, the total time of the time-dependent step in the numerical simulation was set as 1 s. It should be noted that, in this paper, the compressive stress was treated as positive.

The material parameters used in numerical simulation were listed in Table 1, which were cited from the literature (Zhu et al., 2011; Zhang et al., 2016) and fitted according the rock tension and compression experiments. It should be noted that the fluid density is sensitive to the high pressure of the deep *in-situ* environment. Therefore, the fluid density related to pressure was adopted as mixed gas according to the literature (Liu et al., 2017), and the relationship of fluid density and pressure was shown as:

$$\rho_f = 0.77 + 8.45 \times P + 0.176 \times P^2 \tag{17}$$

which is also applicable when the pore pressure P is changed as the fluid pressure P_L.

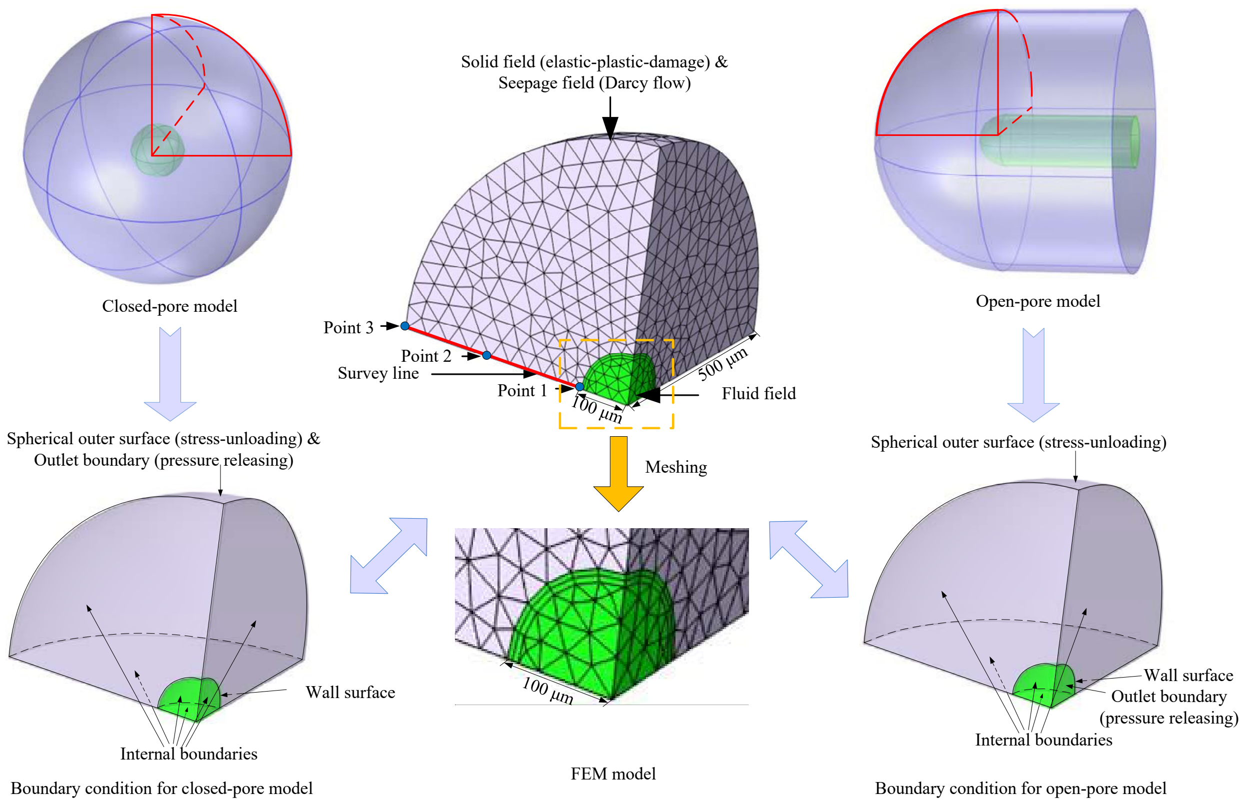

Fig. 3. Schematic diagram of the numerical model.

4. Results and discussion

4.1 Stress distribution under different pore pressures

As mentioned above, the pore pressure could contribute to solid deformation because pores and cracks in the matrix are not fully connected. Thus, the effect of pore pressure on the *in-situ* geostress state is firstly discussed in this section. Because the pore pressure was set to be a constant value and the seepage velocity values were set to be zero in the initial stationary stage of numerical simulations for both the closed-pore model and the open-pore model, the boundary conditions become equivalent for these two models and thus their simulation results are identical. A case with 10 MPa pore pressure and another case without pore pressure were simulated separately under a hydrostatic geostress of 20 MPa. The numerical results corresponding to the *in-situ* geostress state and those after stress unloading alone were shown in Fig. 4. The pore pressure and compression stress were both expressed as positive values.

Fig. 4(a) shows that there is no pore pressure, i.e., the pore pressure is 0 MPa. In this case, the hydrostatic pressure remains 20 MPa. Because the geostress applied on the spherical outer surface is a symmetrical hydrostatic stress, the curves of the first and second principal stress coincide completely, and their values are both nearly 30 MPa on the wall surface due to stress concentration on the pore wall. With the distance from the wall surface increasing, their values decrease to 20 MPa that is equal to the hydrostatic geostress on the spherical outer surface. The third principal stress is 0 MPa on the wall surface and then increases gradually to 20 MPa of geostress. These results agree with the theoretical solution (Grassl and Jirasek, 2006). In Fig. 4(b), when the pore pressure is set to 10 MPa, the hydrostatic pressure is almost 23 MPa because

Table 1. Parameters adopted in numerical simulation.

Parameters	Value
Elasticity modulus E (GPa)	35.0
Poisson's ratio ν	0.25
Matrix density ρ_m (kg/m^3)	2,500
Hardening parameter h_0	0.8
Hardening parameter h_1	2
Hardening parameter b	1.0×10^{-5}
Plastic parameter α	0.2
Plastic parameter R (MPa)	10
Biot's coefficient α_B	0.3
Damage parameter a	5,000
Initial matrix porosity ω_0	0.01
Initial matrix permeability κ_0 (m^2)	$5.0\times10^{-18}\sim$ 5.0×10^{-22}
Fluid kinetic viscosity μ (Pa·s)	1.0×10^{-5}
Fluid compressibility c_r (1/Pa)	1.0×10^{-8}

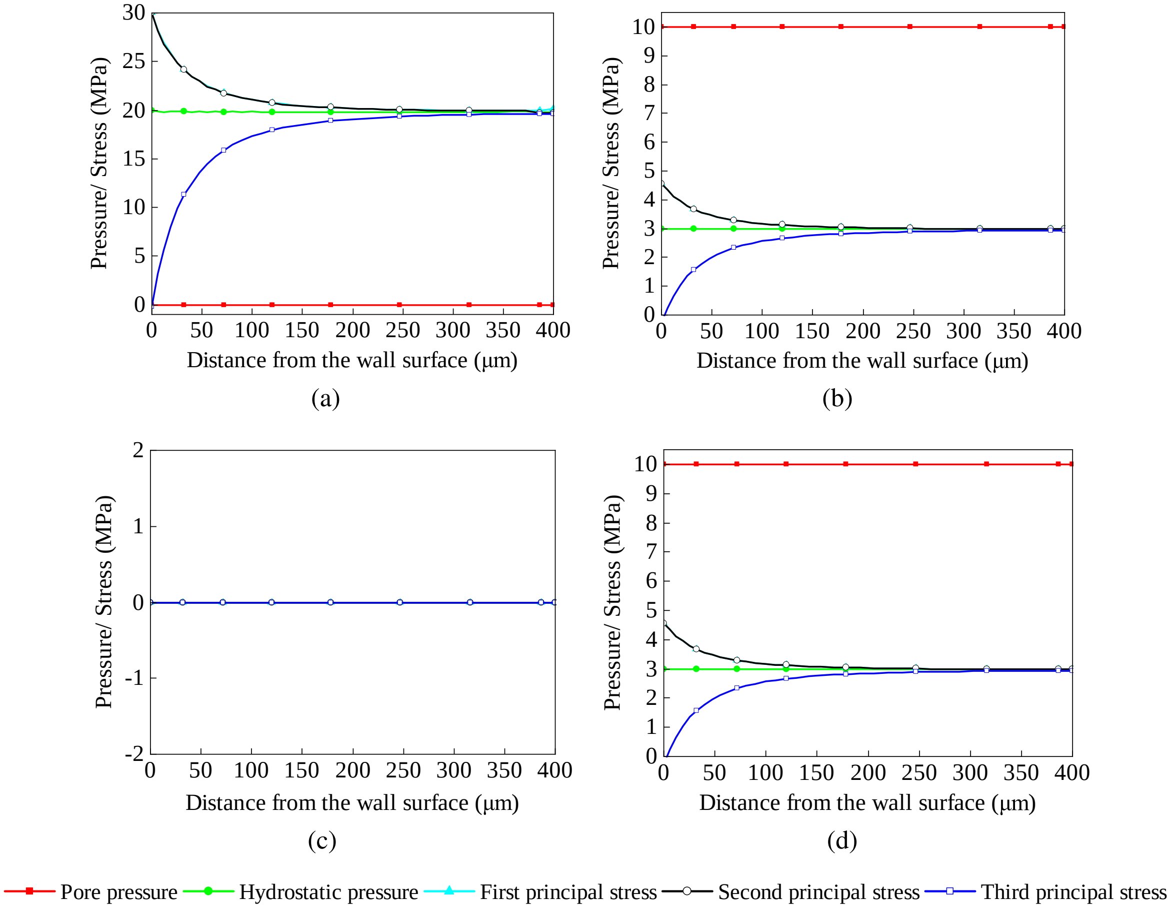

(a) (b) (c) (d)

Fig. 4. Pore pressure and stress distribution curves on the survey line. (a) *In-situ* geostress state ($P = 0$ MPa), (b) *in-situ* geostress state ($P = 10$ MPa), (c) after stress unloading alone ($P = 0$ MPa) and (d) after stress unloading alone ($P = 10$ MPa).

the Biot's coefficient is 0.3. The hydrostatic pressure curve has a slight oscillation near the wall surface, which is inevitable because of the precision of FEM meshing size and coupling calculations step on the wall surface. Such errors are tiny and can be neglected. The curves of the first and second principal stress also coincide completely. The values of the first principal stress and second principal stress are also almost 30.0 MPa on the wall surface but gradually decline to 23 MPa due to the non-zero inner pore pressure. The third principal stress is 10 MPa on the wall surface and then increases to 23 MPa. These results indicate that the stresses near the pore wall are influenced due to the existence of pore and pore pressure. This is no longer hydrostatic stress but has a larger first compressive principal stress component and a smaller third compressive principal stress component. The smallest third compressive principal stress is equal to the pore pressure; hence, the maximum shear stress appears on the pore wall. It can be inferred that such maximum shear stress increases with the growth of hydrostatic geostress but decreases with rising pore pressure.

As shown in Section 3, the displacement boundary was applied to the spherical outer surface to simulate the *in-situ* geostress, and then the given displacement was gradually decreased to simulate the process of stress unloading. The applied displacement on the spherical outer surface became 0 at the end of the stress unloading process. Accordingly, the values of pore pressure, hydrostatic pressure and principal stress were all 0, as shown in Fig. 4(c), when no pore pressure was present. However, if there was a pore pressure of 10 MPa at the beginning, it was still 10 MPa after stress unloading because no seepage was considered, and the hydrostatic pressure was 3 MPa after stress unloading because the Biot's coefficient was 0.3. As plotted in Fig. 4(d), the first and second principal stresses were 4.5 MPa on the wall surface and then declined to 3 MPa with the distance from the wall surface increasing. The third principal stress was 0 MPa on the wall surface and then increased to 3 MPa, which means that the residual pore pressure induces residual compressive stress in the rock matrix even after external stress unloading. The residual stress far away from the pore wall is hydrostatic compressive stress, whose value is dependent on the residual pore pressure and Biot's coefficient. The residual stress near the pore wall appears compressive shear stress whose maximum value is on the pore wall. Thus, it can be inferred that the larger the residual pore pressure, the higher the residual stress.

Table 2. Different conditions for various simulated coring technologies.

Coring technology	Initial permeability	Three internal fluid boundaries		Outer spherical seepage surface	
		Open-pore	Closed-pore	Open-pore	Closed-pore
Pore pressure removal	High $\kappa_0 = 10 \times 10^{-15}$ m^2	Two symmetry planes Outlet (p: $10 \rightarrow 0$ MPa)	Symmetry	Symmetry	Outlet (p: $10 \rightarrow 0$ MPa)
Pore pressure release	Low $\kappa_0 = 5 \times 10^{-18} \sim 5 \times 10^{-22}$ m^2	Two symmetry planes Outlet (p: $10 \rightarrow 0$ MPa)	Symmetry	Symmetry	Outlet (p: $10 \rightarrow 0$ MPa)
Pore pressure preservation	All $\kappa_0 = 5 \times 10^{-15} \sim 5 \times 10^{-22}$ m^2	Outlet ($p = 10$ MPa)	Symmetry	Symmetry	Outlet ($p = 10$ MPa)

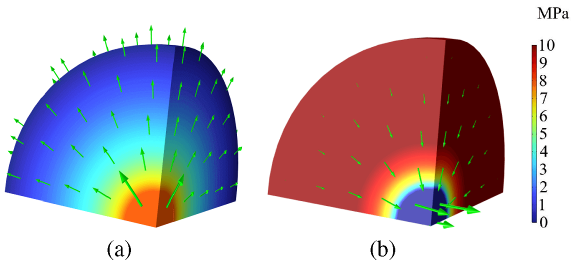

Fig. 5. Fluid pressure and flow direction distribution in the (a) closed-pore model and (b) open-pore model.

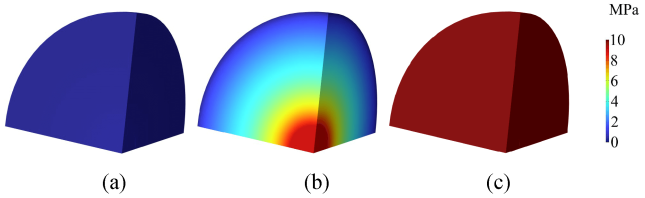

Fig. 6. Three kinds of situations of fluid pressure distribution in the closed-pore model. (a) Pore pressure removal, (b) pore pressure release and (c) pore pressure preservation.

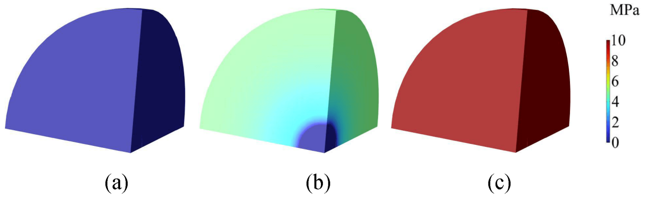

Fig. 7. Three kinds of situations of fluid pressure distribution in the open-pore model. (a) Pore pressure removal, (b) pore pressure release and (c) pore pressure preservation.

4.2 Pore pressure evolution under different coring technologies

As a matter of fact, drilling and coring operations will result not only in stress unloading but also fluid pressure release. To simulate the process of stress unloading, a gradually decreasing displacement was applied on the spherical outer surface, while a gradually decreasing pressure were applied on the outlet surface to simulate the process of fluid pressure release. The results of fluid pressure distribution and flow direction were presented in Fig. 5. Different colors in the model represent various pressures, the arrow indicates the flow direction, and the arrow length represents the fluid velocity. A continuous flow from high pressure to low pressure is formed due to density variation and seepage in both the closed-pore model and the open-pore model. The fluid flows from inside to outside in the closed-pore model, while it flows in the opposite direction in the open-pore model. Besides, it is noticed that the highest fluid velocity appears near the wall surface both in the closed-pore model and the open-pore model.

The various coring technologies can be simulated under different boundary conditions. During the traditional coring process, the fluid pressure on the outlet surface decreases gradually until zero, while during the *in-situ* pressure preserved-coring process, it is fixed to a constant value equal to the *in-situ* pore pressure. The various coring technologies were conceptualized by a series of numerical models. The corresponding simulation methods were listed in Table 2.

The numerical results demonstrate three kinds of situations, namely, pore pressure removal, pore pressure release, and *in-situ* pressure preservation. The distribution of fluid pressure corresponding to the three kinds of situations were drawn in Figs. 6-7 for the closed-pore model and the open-pore model, respectively.

In Figs. 6 and 7, the pore pressure removal situation was obtained under traditional coring of high permeability rock. This indicates that the fluid pressure can be removed suddenly after coring and thus the pressure becomes zero in all models. In Figs. 6 and 7, the pore pressure release situation was acquired under traditional coring of low permeability rock. The results show that the fluid pressure is released partly but cannot be eliminated entirely. The residual fluid pressure presents an uneven distribution that has a radial gradient from the inner pore to the outer surface inside the model. When an *in-situ* pressure-preserved coring was adopted, the *in-situ* pressure-preserved situation was achieved as shown in Figs. 6 and 7. This indicates that the fluid pressure is retained with a uniformly distributed value in all models, which remains equal to the initial *in-situ* pore pressure.

The above various situations are the result of an important factor, the permeability of rock material. The fluid pressure will be removed completely in the case that the permeability is large enough to allow the fluid to flow out completely. However, the permeability is usually small in a deep *in-situ* environment because of intense sedimentation. Therefore, the pore pressure removal situation rarely appears in deep rocks, while the pore pressure release situation is common in the most of the current coring technologies. This means that the fluid pressure inside rocks will be unevenly distributed after traditional coring, inevitably causing non-uniform stress and even damage as discussed in later in Section 4.4. Such non-uniform residual fluid pressure in rock cores will likely result in the failure phenomena of coring, such as discing, surface spalling and even thorough fragmentation. Further laboratory tests based on these traditional coring samples will reveal some distortion results that deviate from the actual *in-situ* conditions. If an *in-situ* pressure-preserved coring was conducted, the fluid pressure would be compulsorily kept unchanged even after stress unloading. The initial uniform fluid pressure will remain uniform and thus avoid producing uneven extra stress and damage. Such pore pressure-preserved situation is independent of the rock permeability because the seepage is prevented after supplying an artificial outer pressure that has eliminated the pressure difference inside the rock. Thus, it can be speculated that *in-situ* pressure-preserved coring will be conducive to both the successful coring of complete samples and credible testing based on *in-situ* conditions.

4.3 Permeation pressure distribution and evolution due to coring

In the process of coring with stress-unloading and the pore pressure-release effect, the fluid always flows in the pore and results in seepage in the matrix. The fluid pressure in the fluid field can still be called as pore pressure, while the fluid pressure in the seepage field will be called as permeation pressure. It needs to be stated that the traditional term pore pressure is considered at the macroscale, which refers to fluid pressure in different kinds of pores at all scales. Herein, the term permeation pressure implies a pore pressure that can be treated as a continuum field variable without considering its physical positions. Based on the above analysis, matrix permeability is a key factor influencing the fluid seepage. In most cases, the fluid pressure in actual rocks cannot be completely released suddenly. Hence, it is crucial to conduct research on permeation pressure distribution and evolution for pore pressure release situations.

To study the spatial distribution of permeation pressure after coring, a pre-arranged survey line was used in the models. The data of various time on each monitoring point were taken to analyze the temporal evolution law of permeation pressure in the models. Three points were selected and monitored as illustrated in Fig. 3. These points are arranged on the pore wall surface, the middle of the survey line and the outer spherical surface, separately.

4.3.1 Effect of matrix permeability

The permeability of matrix affects the distribution and evolution of permeation pressures. Different permeabilities were simulated by a serial of numerical models. The results on the survey line and the monitoring points were plotted in Fig. 8 and Fig. 9 for the closed-pore model and the open-pore model, respectively. The zero of the abscissae indicates the position of the wall surface.

The permeation pressure distribution curves on the survey line in closed-pore models with different permeabilities after stress unloading and pore pressure release were plotted in Fig. 8(a). The permeation pressure is almost 0 MPa when $\kappa_0 = 5 \times 10^{-18}$ m^2, which means that pore pressures had been almost completely released. With the permeability decreasing, an obvious pressure gradient field is formed in the model. For example, when $\kappa_0 = 5\mathrm{e} \times 10^{-22}$ m^2, the permeation pressure is almost 9 MPa on the wall surface and decreases to 0 MPa with the distance from the wall surface increasing. Figs. 8(b) and Fig. 8(c) show the permeation pressure evolution on the monitoring points in closed-pore models at different times. The permeation pressure on the spherical outer surface in Fig. 8(c) reduces from 10 to 0 MPa under every permeability because it is set as a boundary condition. The permeation pressure on the pore wall surface in Fig. 8(b) decreases from 10 to 0 MPa when $\kappa_0 = 5 \times 10^{-18}$ m^2 but only decreases to 9 MPa when $\kappa_0 = 5 \times 10^{-22}$ m^2.

The seepage velocity distribution curves on the survey line in closed-pore models with different permeabilities after stress unloading and pore pressure release were plotted in Fig. 8(d), and the seepage velocity evolution at the monitoring points at different times were plotted in Figs. 8(e) and 8(f). The seepage velocity near the cavity is higher than that on the outer surface because the fluid mass remains conserved between the inflow from the smaller closed-pore wall and the outflow from the larger outer surface. In addition, the seepage velocity decreases obviously on the wall surface with the permeability decreasing. For example, when $\kappa_0 = 5 \times 10^{-18}$ m^2, the seepage velocity is almost 500 μm/s on the wall surface and decreases to 50 μm/s with the distance from the wall surface increasing, but when $\kappa_0 = 5 \times 10^{-22}$ m^2, the seepage velocity is almost 0 μm/s. It can be noticed that the seepage velocity increases slowly at the beginning of coring and then rapidly becomes larger near the end of coring. Such trends are different to those of permeation pressure variations, which are approximately linear. The reason is that the decreasing level on the inner pore wall surface is smaller than that on the outer spherical surface, so the permeation pressure gradient becomes greater over time and the seepage velocity becomes accordingly larger. However, the value of seepage velocity is controlled mainly by the magnitude of permeability rather than the variation of permeation pressure gradient, because the permeability might change by several orders but the order of permeation pressure gradient shows no change. The larger the permeability, the lower the permeation pressure drop over time and the quicker the seepage velocity becomes, which means that pore fluids will be released completely. On the contrary, the smaller the permeability, the less the permeation pressure drops over time and the smaller the seepage velocity becomes, which means that pore fluids are hard to be released and thus will be sealed in rocks at a certain pressure.

The permeation pressure distribution curves of open-pore

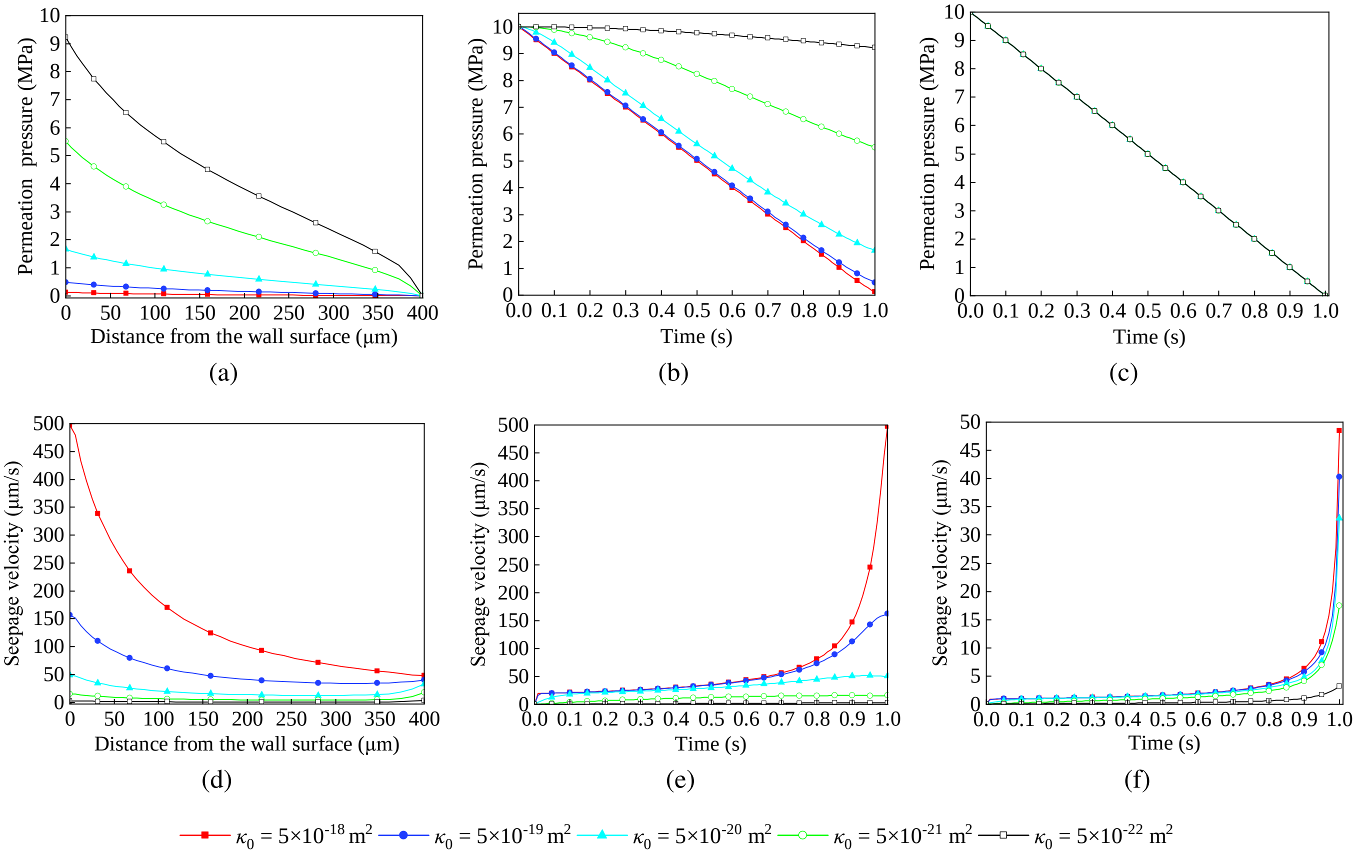

(a) (b) (c)

(d) (e) (f)

Fig. 8. Permeation pressure and seepage velocity curves of the closed-pore model. (a) Permeation pressure on the survey line, (b) seepage velocity on the survey line, (c) permeation pressure on the pore wall surface, (d) seepage velocity on the pore wall surface, (e) permeation pressure on the spherical outer surface and (f) seepage velocity on the spherical outer surface.

models on the survey line with different permeabilities after stress unloading and pore pressure release were plotted in Fig. 9(a). The position of permeation pressure drops in open-pore models is opposite to that in closed-pore models. The pore fluids in closed cavities escape by seepage through the matrix from inner cavities to the outer surface, such that the permeation pressure on the outer surface eventually becomes zero and that on the inner pore wall retains a certain value that depends on the magnitude of permeability. The pore fluids in open cavities flow from inner cavities to outer fissures, resulting in seepage through the matrix from the spherical surface to the pore wall, which direction is opposite to the seepage direction in the closed-pore model and means that the permeation pressure on the pore wall eventually becomes zero and that on the spherical surface retains a certain value that depends on the magnitude of permeability. Nevertheless, the trends of permeation pressure drops under different permeabilities are similar. The permeation pressure is almost 0 MPa when $\kappa_0 = 5\times10^{-18}$ m^2, while it undergoes a drop from 5 MPa on the spherical surface to 0 MPa on the pore wall surface when $\kappa_0 = 5\times10^{-22}$ m^2. However, the permeation pressure decline in open-pore models occurs near the pore wall, which is different from the uniform decrease in permeation pressure along the whole zone in closed-pore models. Fig. 9(c) show that the smaller the permeability, the less the permeation pressure drops over time. Such trend is the same to that in closed-pore models. The permeation pressure on the pore wall surface drops from the initial 10 to 0 MPa under any permeability, while the permeation pressure of monitoring point 3 on the spherical surface drops to only about 5 MPa when the permeability is $\kappa_0 = 5\times10^{-22}$ m^2.

The seepage velocity on the survey line and the monitoring points in open-pore models were plotted in Figs. 9(d)-9(f). The seepage velocity in open-pore models is far smaller than that in closed-pore models because in open-pore models, the permeation pressure gradient is relatively small, as shown in Fig. 9(a). The seepage velocity near the cavity is greater than that on the outer surface. This trend is similar to that in the closed-pore model owing to mass conservation. It can still be noticed that the smaller the permeability, the smaller the overall seepage velocity is. Although the seepage velocity near the pore wall presents a reverse trend with the permeability ultimately increasing, as shown in Fig. 9(d), this is due to the fact the drop in permeation pressure occurs in a zone near the pore wall and there exists a relatively large permeation pressure gradient near the pore wall under low permeability, as shown in Fig. 9(a). The impact of such contradiction can be neglected because it is limited to a small zone near the pore wall. However, the variations in seepage velocity over time are distinct from that in the closed-pore model and become

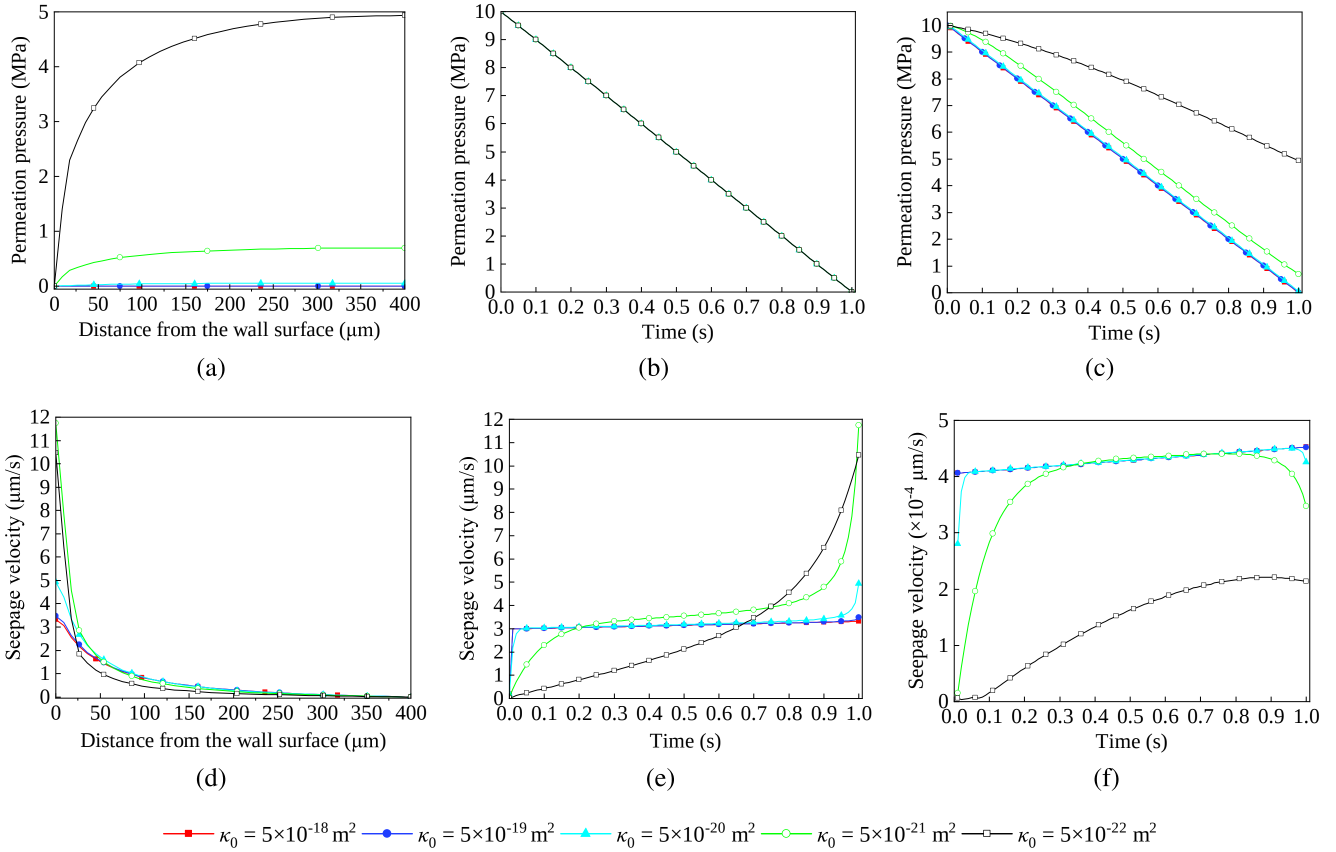

(a) (b) (c)

(d) (e) (f)

Fig. 9. Permeation pressure and seepage velocity curves of the open-pore model. (a) Permeation pressure on the survey line, (b) seepage velocity on the survey line, (c) permeation pressure on the pore wall surface, (d) seepage velocity on the pore wall surface, (e) permeation pressure on the spherical outer surface and (f) seepage velocity on the spherical outer surface.

complex. This means an S-shaped three-stage curve that highly depends on the permeability. In the first stage, the seepage velocity increases rapidly to a certain value at a decreasing rate. Then, the seepage velocity exhibits a very slight increase with small constant rates in the second stage. At last, the seepage velocity presents an accelerating variation that is still increased near the pore wall but decreased far away from it in the third stage. When the permeability is large enough, such as $\kappa_0 = 5 \times 10^{-18}$ m^2, the first stage is too short to be observed and the third stage fails to occur, i.e., the seepage velocity almost remains a slightly increasing value. This indicates that fluids flow steadily from matrix to cavities and will be predictably removed in the end. With the permeability decreasing, the first and third stage becomes longer and the second stage becomes shorter. When the permeability is small enough, such as $\kappa_0 = 5 \times 10^{-22}$ m^2, the second stage fails to occur. The seepage velocity near the pore wall increases gradually at an accelerating rate, which can be regarded as being in third stage, while the seepage velocity far away from the pore wall increases gradually at a slowing rate, which can be regarded as being in first stage, and then decreases gradually at a growing rate, which can be regarded as being in short third stage. The drop in seepage velocity far away from the pore wall under low permeability indicates that fluids flows have been restricted and will predictably cease in the end.

Both the closed-pore models and the open-pore models have illustrated that the matrix permeability highly affects the distribution and evolution of permeation pressures. In closed-pore models, seepage in the matrix is driven by inner high pore pressure in closed cavities and its direction is from inner cavities to outer surface, and a uniform decrease in permeation pressure arises from inner cavities to the outer surface. At last, faster seepage velocity occurs, which is mainly attributed to the greater gradient of permeation pressures. In open-pore models, seepage in the matrix is driven by pore fluids flowing away from open cavities, with the direction of spherical surface to pore wall, and a relative sharp decrease in permeation pressure arises near the pore wall. Variations in the seepage velocity over time present a complex S-shaped three-stage curve that highly depends on the permeability: The seepage velocity might even decrease overall due to lower permeability. Although the driven mechanism of seepage in the two kinds of model is distinct, the impact of permeability on seepage is consistent. The matrix with lower permeability can restrict the seepage of fluid and thus result in larger permeation pressure gradient in spatial distribution and slower seepage velocity, which means that the pore pressure is hard to be released, so smaller pressure drops appear over time. The matrix with larger permeability can be conducive to the seepage of fluid and thus form a smaller permeation pressure

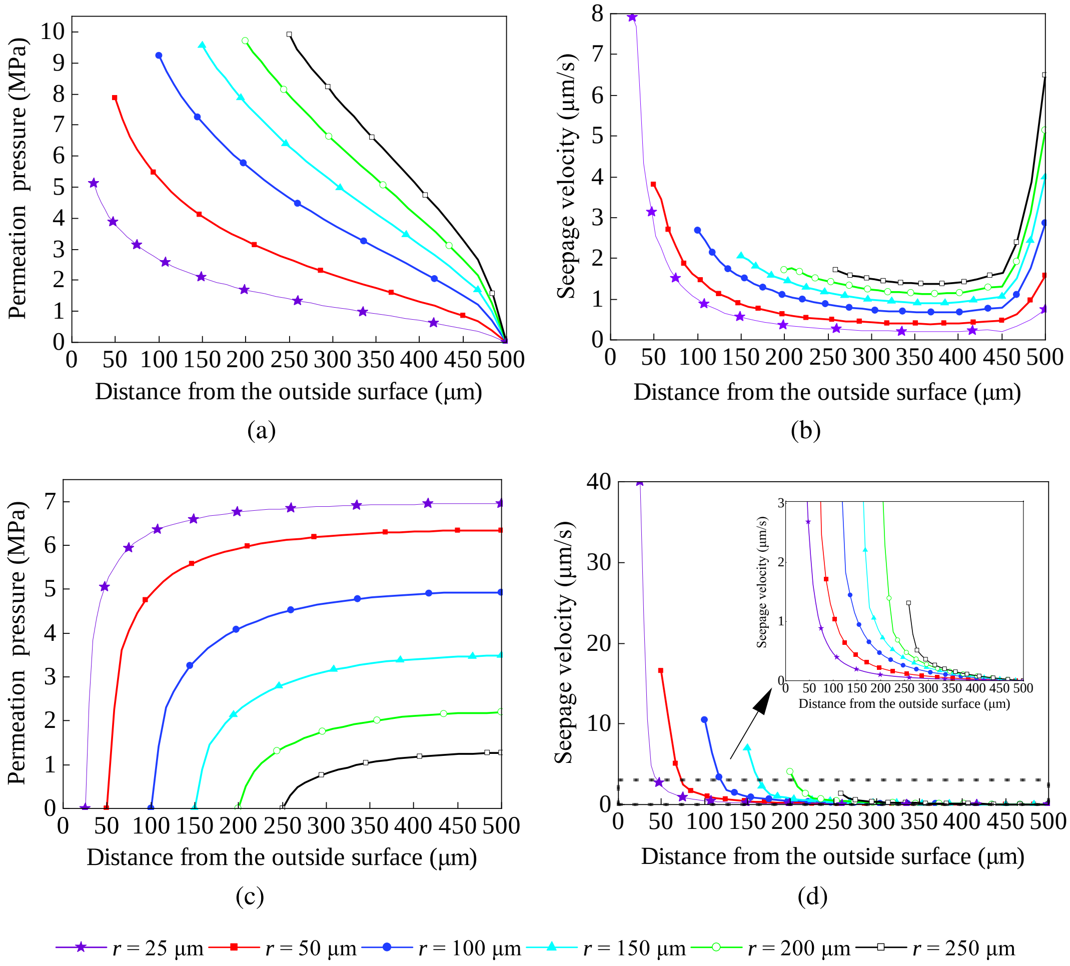

(a) (b) (c) (d)

Fig. 10. Permeation pressure curves and seepage velocity curves on the survey line for different cavity radii with $\kappa_0 = 5 \times 10^{-22}$ m^2. (a) and (b) Closed-pore mode, (c) and (d) open-pore model.

gradient in spatial distribution and quicker seepage velocity, which means that the pore pressure will be easily released, making greater pressure drops appear over time. This implies that lower permeability can cause higher residual permeation pressure in the rock matrix.

4.3.2 Effect of permeation pressure gradient represented by cavity radius

The seepage velocity was associated with the gradient of permeation pressure. To examine the effect of different gradients of permeation pressure, a serial of numerical models with various radii (r) of cavity were simulated. Based on the original model with an outer radius of 500 μm and a permeability $\kappa_0 = 5 \times 10^{-22}$ m^2, the cavity radius was set to different values separately, including $r = 25$, 50, 100, 150, 200, 250 μm. The boundary conditions remained unchanged, and thus the gradients of permeation pressure were altered because the distance along which the pressure drops was changed. The results of permeation pressure and seepage velocity on the survey line with different cavity radii after stress unloading and pore pressure release were plotted in Fig. 10, respectively. The horizontal axis denotes the distance from the center of sphere, which means the value 0 represents the location of the center of sphere, and the value 500 μm represents the location of the spherical outer surface. The curves corresponding to the various cavity radii start from different positions.

The permeation pressure curves in the closed-pore model are overall reclining S-shaped, as shown in Fig. 10(a). When the cavity radius is larger, the permeation pressure on the pore wall surface is higher. For example, the permeation pressure on the pore wall surface is almost 5 MPa when $r = 25$ μm, but it is almost 10 MPa when $r = 250$ μm. On the spherical outer surface, the permeation pressure of all curves declines to 0 MPa. A larger gradient of permeation pressure leads to a higher seepage velocity. Meanwhile, the reclining S-shaped curves of permeation pressure yield the seepage velocity's U-shaped curves. From Fig. 10(b), the seepage velocity decreases from a relatively large value on the wall surface to a minimum value, and then increases to a higher value on the spherical outer surface. For instance, when $r = 150$ μm, the seepage velocity is almost 2 μm/s and decreases to 1 μm/s in the middle of the survey line, and then increases to almost 4 μm/s on the spherical outer surface.

The permeation pressure in the open-pore model decreases

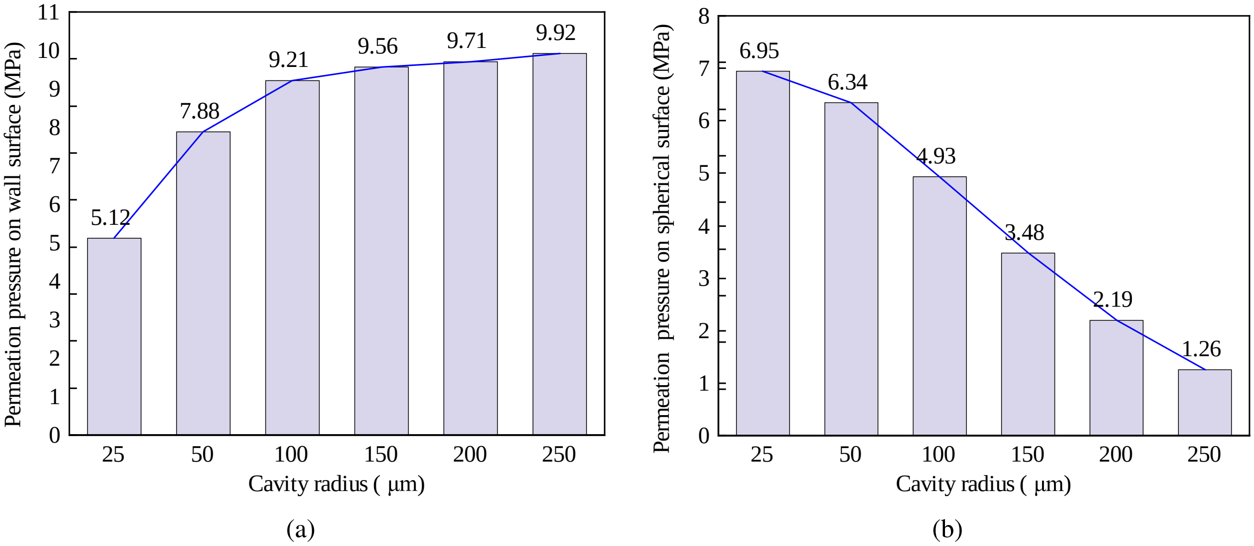

Fig. 11. Permeation pressure under different cavity radii with $\kappa_0 = 5 \times 10^{-22}$ m^2. (a) Closed-pore model and (b) open-pore model.

from a high value on the spherical outer surface to zero on the pore wall surface, as shown in Fig. 10(c). The permeation pressure on the spherical outer surface becomes smaller with increasing cavity radius. For example, the permeation pressure on the spherical outer surface is almost 7 MPa when $r = 25$ μm, but it is merely 1 MPa when $r = 250$ μm. The seepage velocity on the wall surface becomes higher with decreasing cavity radius. From Fig. 10(d), it can be deduced that the seepage velocity value on the wall surface is almost 40 μm/s when $r = 25$ μm, but it is merely 2 μm/s when $r = 250$ μm. On the spherical outer surface, the seepage velocity of all curves declines to almost 0, because the permeation pressure has a larger gradient near the wall surface and remains almost identical far away from the cavity.

Since the boundary conditions on the pore wall and spherical surface remain unchanged, the effect of cavity size on the permeation pressure distribution and evolution is mainly attributed to the gradient of permeation pressure. However, opposing trends were noticed between the closed-pore models and open-pore models. The permeation pressure gradient in the matrix with larger closed cavities is higher than that with smaller closed cavities, while the permeation pressure gradient in the matrix with larger open cavities is smaller than that with smaller open cavities. Besides, a relatively sharper permeation pressure gradient arises near the seepage outlet, which is the spherical outer surface in closed-pore models or the pore wall surface in open-pore models, and accordingly the largest value of seepage velocity arises on the outlet boundary on the whole. These opposing trends were also noticed in that larger closed cavities lead to higher outlet seepage velocity while larger open cavities lead to lower velocity. This indicates that the higher residual permeation pressure and seepage velocity in the rock matrix will be caused by a larger closed cavity or a smaller open cavity.

Fig. 11 shows the residual maximum permeation pressure in the matrix, which arises on the pore wall in the closed-pore model while on the spherical surface in the open-pore model. Overall, the decrease in permeation pressure is linear with the increase in cavity size in the open-pore model, which means that the effect of open cavity size is uniform. However, the increasing rate of permeation pressure slows down when the cavity radius exceeds 100 μm. This means that the effect of closed cavity size is nonlinear and there exists a threshold cavity size, below which the effect is overall linear but becomes weak beyond it. In addition, Fig. 11(a) shows that some exceptions of seepage velocity distribution occur when the cavity sizes are smaller than this threshold, where the largest value of seepage velocity arises on the inlet pore wall but not at the outlet spherical surface. On the contrary, when cavity sizes are larger than this threshold, the largest value of seepage velocity arises on the outlet spherical surface as mentioned above. This implies that the impact mechanism of cavity size is highly complex under the stress-flow coupling process. Once the cavity is too small, the impact of stress concentration cannot be neglected. However, if the cavity is large enough, the permeation pressure gradient will no longer increase more greatly with shorter seepage path because of the limitation of flow mass conservation and stress balance between inlet and outlet. Under specific material parameters and boundary conditions, a cavity size threshold might be determined. Nevertheless, the overall trends of cavity size effect have been revealed, and the impact of permeation pressure gradient on the permeation pressure distribution and evolution can be preliminarily learned.

4.4 Stress distribution and coring-induced inner damage under different coring technologies

In order to clarify the inner damage mechanisms during coring with stress unloading and pore pressure release or preservation, the inner damage distributions were calculated.

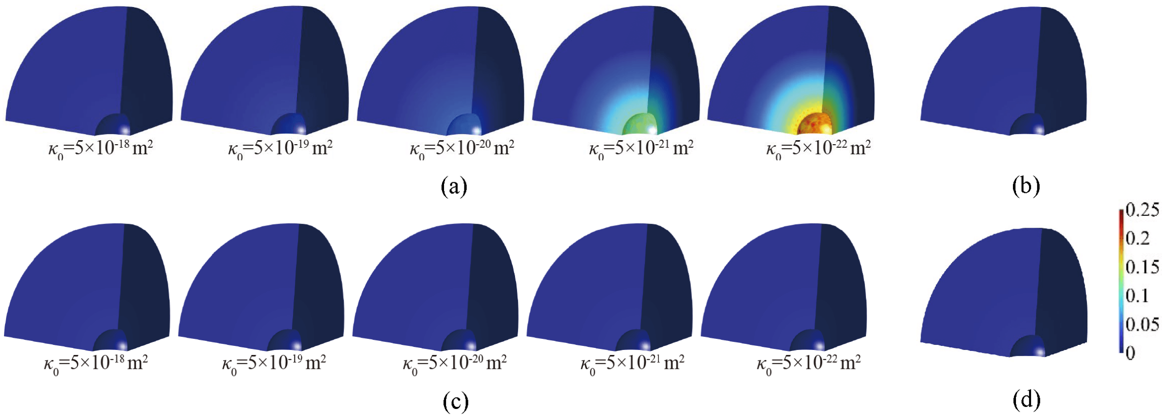

Fig. 12. Damage distribution in the closed-pore model and the open-pore model after coring. (a) Pore pressure release in the closed-pore model with different permeability, (b) pore pressure preservation in the closed-pore model, (c) pore pressure release in the open-pore model with different permeability and (d) pore pressure preservation in the open-pore model.

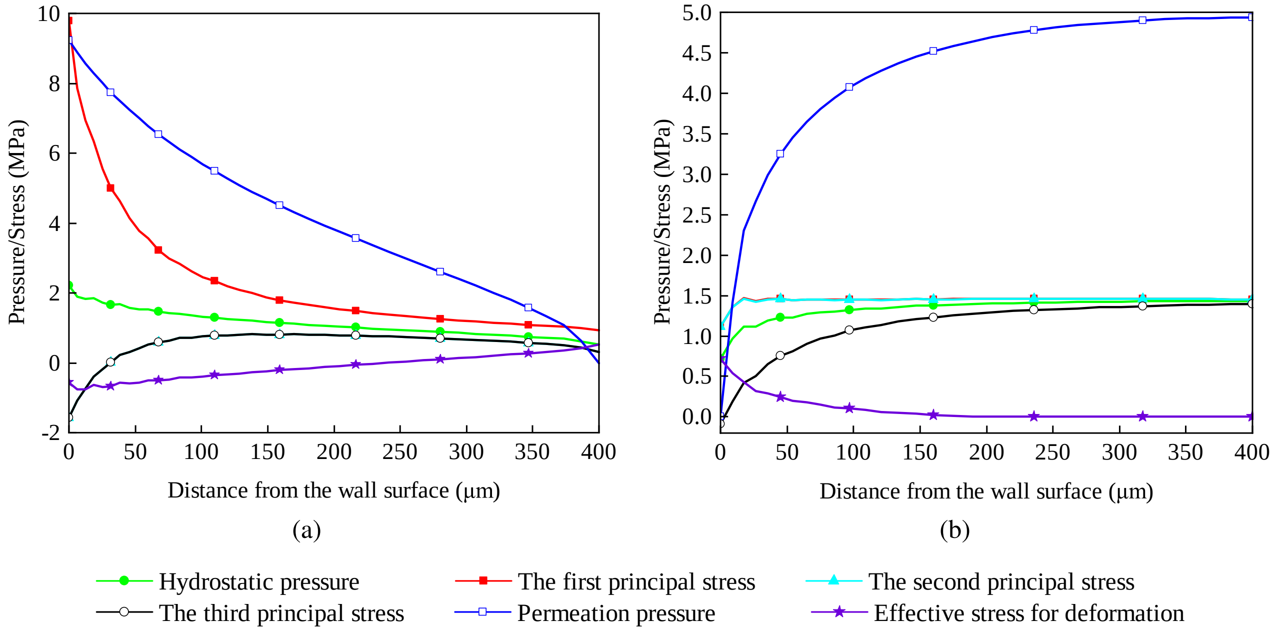

Fig. 13. Stress distribution curves after coring with $\kappa_0 = 5 \times 10^{-22}$ m^2 and $r = 100$ μm. (a) Closed-pore model and (b) open-pore model.

According to the damage variable defined in Eq. (3), the damage values on each node were computed based on the corresponding tensile volume strain. If the volume strain was compressive, it was set as 0 in Eq. (3). The damage distribution in closed-pore models and open-pore models were presented in Fig. 12. The maximum damage value and its position could be determined from the computation results.

The damage occurs in the closed-pore model mainly near the pore wall surface. Both the damage value and the damage zone increase with decreasing permeability. The maximum damage value is just about 0.004 when $\kappa_0 = 5 \times 10^{-18}$ m^2, while it increases to 0.231 when $\kappa_0 = 5 \times 10^{-22}$ m^2 and the damage zone also enlarges obviously. It can be seen from Fig. 12 that the extra damage occurs in the closed-pore model under the pore pressure-released coring but no damage arises under the pore pressure-preserved coring. Beyond that, it also could be seen from Fig. 12 that no damage occurs in the open-pore model. Overall, the coring-induced inner damage will occur near the closed cavities under traditional pore pressure-released coring.

Fig. 13 shows the stress distribution curves on the survey line in the pore pressure released model with a permeability $\kappa_0 = 5 \times 10^{-22}$ m^2 after coring. The hydrostatic pressure becomes uneven in the matrix under lower permeability; its value on the pore wall surface is larger than that on the spherical outer surface. The second principal stress and the third principal stress near the pore wall surface are both tensile stresses. The tensile stress can lead to expansive deformation and easily result in damage because of the tension-compression asymmetry feature of rock materials (Edwards, 1951). The

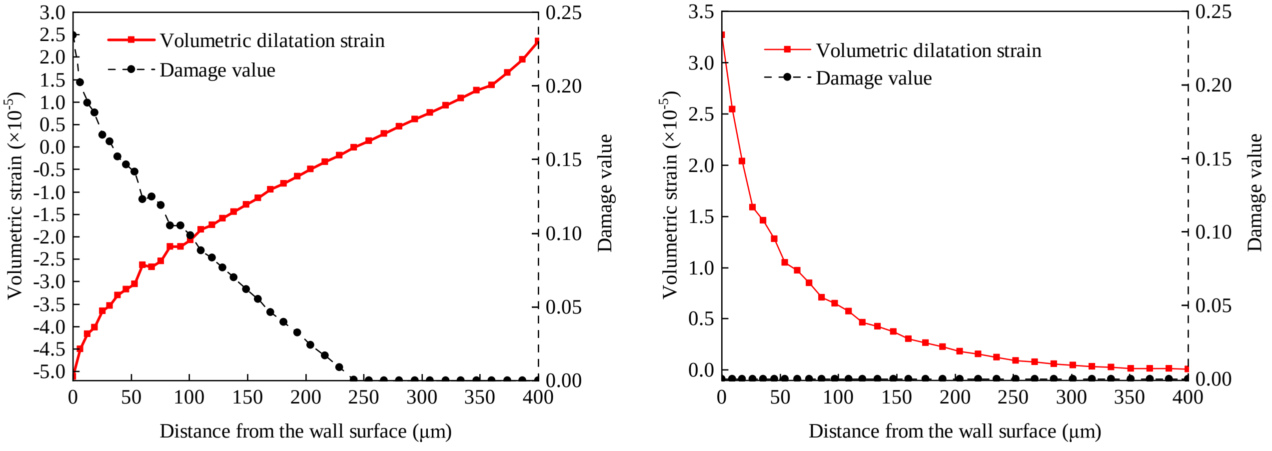

(a)

(b)

Fig. 14. Damage distribution curves after coring with $\kappa_0 = 5 \times 10^{-22}$ m^2 and $r = 100$ μm. (a) Closed-pore model and (b) open-pore model.

permeation pressure is just the same to that of $\kappa_0 = 5 \times 10^{-22}$ m^2 in Figs. 8(a) and 9(a). As mentioned above in Section 2.2.1, the pore pressure effect was treated as an additive stress and thus the total stresses were calculated according to Eq. (1). The effective stress that results in matrix deformation could be derived by subtracting the permeation pressure multiplied by Biot's coefficient from the total stress according Eq. (1). The effective hydrostatic stresses were computed and plotted in Fig. 13 for the closed-pore model and open-pore model, and the corresponding volumetric strain from numerical simulation results were plotted in Fig. 14. It can be noticed that the effective hydrostatic stress and the volumetric strain for the closed-pore model are negative near the pore wall, which leads to volume expansion due to tension. Therefore, the damage value could be calculated according to Eq. (3), which is plotted in Fig. 14. On the pore wall, the volume expansion is greatest and thus the damage value is the maximum. With the distance from the pore wall increasing, the damage value decreases gradually. However, the effective hydrostatic stress and the volumetric strain for the open-pore model are always positive near pore wall and then decrease to almost zero, which means that no damage occurs.

In general, the *in-situ* stress and pressure environments might be restored prior to laboratory tests of coring samples, so that some actual responses of deep rock can be simulated and examined. Those damaged coring samples will suffer second damage due to stress and pressure restoration before continuing the required tests. Besides, the traditional samples fail to retain the *in-situ* pore pressure and are characterized by non-uniformly distributed permeation pressure and stress, whose value and distribution are specific to the actual *in-situ* environments. This can lead to the distortion of the laboratory test results, misleading the assessment for the mechanical properties of deep rocks. On the contrary, the permeation pressure is distributed evenly inside the matrix under pore pressure-preserved coring, and the residual stress distribution is similar to that of the *in-situ* environment. No extra damage and tensile stress arise when the pore pressure is preserved. These results are sufficient to illustrate the importance of pore pressure-preserved coring, which will be conducive to preventing the further damage of coring samples and retain the *in-situ* high pressure and high stress.

5. Conclusions

In this paper, a closed-pore model and an open-pore model were established at the mesoscopic scale for numerical simulation under stress-flow coupling. The distribution and evolution of fluid pressure and solid stress due to different coring technologies were obtained and compared. The coring-induced inner damage was examined and its influence factors were determined. The significance of *in-situ* pore pressure-preserved coring was demonstrated. The main conclusions could be drawn as follows:

1) An elastic-plastic-damage model was proposed to reflect the tensile damage effect on both the elasticity tensor and plastic hardening function. The coupling mechanism among the elastic-plastic-damage solid field, Darcy's seepage field and laminar flow filed were revealed, and the corresponding calculation formulas were put forward.
2) The pore pressure distribution after coring could be classified into three situations: Pore pressure removal, pore pressure release, and *in-situ* pressure preservation. The pore pressure release situation is most common in the current traditional coring process because the rock matrix is usually of low permeability. In this scenario, the *in-situ* high pore pressure cannot be removed suddenly and lead to a non-uniformly distributed permeation pressure and residual stress field inside rock samples. Lower permeability, larger closed cavities or smaller open cavities will result in the higher residual permeation pressure and stress in the rock matrix.
3) The coring-induced inner damage arises mainly nearby

closed cavities during the traditional coring of deep rocks with low permeability. Such damage is induced by extra tensile stress that arises when the pore pressure is released incompletely. Both the degree of damage and the damage zone are increased with decreasing permeability.

4) No extra damage arises either in closed-pore structures or open-pore structures under the *in-situ* pore pressure-preserved coring, which produce evenly distributed permeation pressure and causes residual stress distribution similar to that of the *in-situ* environment. Hence, deep coring with *in-situ* pore pressure preservation is conducive to preventing the further damage of coring samples and retain *in-situ* high pressure and high stress. It can be inferred that conducting pore pressure-preserved coring is important to avoid the distortion of the laboratory test results for coring samples.

The current work illustrates some preliminary conclusions on coring-induced damage by a serial of simplifying conceptualized model, in which a numerical simulation for stress-flow coupling has been proved to be workable and applicable in similar studies. However, there are always extremely complex conditions in the underground environment, where the extra damage during coring could be indeed severe and inevitable. Nevertheless, the current researches have demonstrated that the *in-situ* pore pressure-preserved coring technology is expected to be a feasible method with great progress to minimize the potential impacts of coring.

Acknowledgements

This work was supported by the National Natural Science Foundation of China (No. 51827901), the Innovative Research Group Project of the National Natural Science Foundation of China (No. 52121003), and the National Key Research and Development Program of China (No. 2022YFC2904102). The authors are also thankful to the editor and anonymous reviewers for their valuable advice.

Supplementary file

https://doi.org/10.46690/ager.2024.12.03

Conflict of interest

The authors declare no competing interest.

References

Bruning, T., Karakus, M., Nguyen, G. D., et al. An experimental and theoretical stress-strain-damage correlation procedure for constitutive modelling of granite. International Journal of Rock Mechanics and Mining Sciences, 2019, 116: 1-12.

Cao, Z., Gu, Q., Huang, Z., et al. Risk assessment of fault water inrush during deep mining. International Journal of Mining Science and Technology, 2022, 32(2): 423-434.

Chao, Z., Ma, G., He, K., et al. Investigating low-permeability sandstone based on physical experiments and predictive modeling. Underground Space, 2021, 6(4): 364-378.

Chen, X., Xue, S., Yuan, L. Coal seam drainage enhancement using borehole presplitting basting technology-a case study in huainan. International Journal of Mining Science and Technology, 2017, 27(5): 771-775.

Di, Q., Li, P., Zhang, M., et al. Three-dimensional theoretical analysis of seepage field in front of shield tunnel face. Underground Space, 2022, 7(4): 528-542.

Du, C., Sun, L., Guo, Y., et al. Experimental study on the coal damage characteristics of adsorption-instantaneous pressure relief in coal containing gases with different adsorption characteristics. Applied Sciences, 2019, 9(23): 5223.

Edwards, R. H. Stree concentrations around spheroidal inclusions and cavities. Journal of Applied Mechanics, 1951, 18(1): 19-30.

Gao, M., Chen, L., Fan, D., et al. Principle and technology of coring with *in-situ* pressure and gas maintaining in deep coal mine. Journal of China Coal Society, 2021, 46(3): 885-897. (in Chinese)

Golparvar, A., Zhou, Y., Wu, K., et al. A comprehensive review of pore scale modeling methodologies for multiphase flow in porous media. Advances in Geo-Energy Research, 2018, 2(4): 418-440.

Grassl, P., Jirasek, M. Damage-plastic model for concrete failure. International Journal of Solids and Structures, 2006, 43(22-23): 7166-7196.

Hokka, M., Black, J., Tkalich, D., et al. Effects of strain rate and confining pressure on the compressive behavior of kuru granite. International Journal of Impact Engineering, 2016, 91: 183-193.

La Spina, A., Foerster, C., Kronbichler, M., et al. On the role of (weak) compressibility for fluid-structure interaction solvers. International Journal for Numerical Methods in Fluids, 2020, 92(2): 129-147.

Liu, S., Wang, D., Yin, G., et al. Experimental study on the microstructure evolution laws in coal seam affected by temperature impact. Rock Mechanics and Rock Engineering, 2020, 53(3): 1359-1374.

Liu, S., Zhang, Y., Chi, Y., et al. Density characteristics of CO_2-CH_4 binary mixtures at temperatures from (300 to 308.15) K and pressures from (2 to 18) MPa. The Journal of Chemical Thermodynamics, 2017, 106: 1-9.

Li, W., Liu, S., Osher, S. Controlling conservation laws ii: Compressible navier-stokes equations. Journal of Computational Physics, 2022, 463: 111264.

Li, X., Cao, W., Su, Y. A statistical damage constitutive model for softening behavior of rocks. Engineering Geology, 2012, 143-144: 1-17.

Ma, Y., Cai, X., Yun, L., et al. Practice and theoretical and technical progress in exploration and development of shunbei ultra-deep carbonate oil and gas field, tarim basin, NW China. Petroleum Exploration and Development, 2022, 49(1): 1-20.

Shen, Y., Ge, H., Zhang, X., et al. Impact of fracturing liquid absorption on the production and water-block unlocking for shale gas reservoir. Advances in Geo-Energy Research, 2018, 2(2): 163-172.

Tang, X., Ripepi, N., Stadie, N. P., et al. A dual-site langmuir equation for accurate estimation of high pressure deep shale gas resources. Fuel. 2016, 185: 10-17.

Wu, Z., Sun, Z., Shu, K., et al. Mechanism of shale oil displacement by CO_2 in nanopores: A molecular dynamics simulation study. Advances in Geo-Energy Research, 2024, 11(2): 141-151.

Xie, H., Gao, M., Zhang, R., et al. Study on concept and progress of in situ fidelity coring of deep rocks. Chinese Journal of Rock Mechanics and Engineering, 2020, 39(5): 865-876. (in Chinese)

Xie, H., Li, C., He, Z., et al. Experimental study on rock mechanical behavior retaining the in situ geological conditions at different depths. International Journal of Rock Mechanics and Mining Sciences, 2021a, 138: 104548.

Xie, H., Liu, T., Gao, M., et al. Research on *in-situ* condition preserved coring and testing systems. Petroleum Science, 2021b, 18(6): 1840-1859.

Yang, D., Qi, X., Chen, W., et al. Numerical investigation on the coupled gas-solid behavior of coal using an improved anisotropic permeability model. Journal of Natural Gas Science and Engineering, 2016, 34: 226-235.

Yan, P., Lu, W., He, Y., et al. Coring damage mechanism of the Yan-tang group marble: combined effect of stress redistribution and rock structure. Bulletin of Engineering Geology and the Environment, 2016, 75: 1701-1716.

Zha, E., Zhang, Z., Zhang, R., et al. Long-term mechanical and acoustic emission characteristics of creep in deeply buried jinping marble considering excavation disturbance. International Journal of Rock Mechanics and Mining Sciences, 2021, 139: 104603.

Zhang, J., Hou, X., Zhou, G., et al. Quantifying and controller determination of shale matrix compressibility: Implications for pore structure and gas flow behavior analyses. Natural Resources Research, 2023, 32(5): 2095-2114.

Zhang, J., Xu, W., Wang, H., et al. A coupled elastoplastic damage model for brittle rocks and its application in modelling underground excavation. International Journal of Rock Mechanics and Mining Sciences, 2016, 84: 130-141.

Zhang, L., Huang, M., Xue, J., et al. Repetitive mining stress and pore pressure effects on permeability and pore pressure sensitivity of bituminous coal. Natural Resources Research, 2021, 30(6): 4457-4476.

Zhang, T., Yu, L., Su, H., et al. Experimental and numerical investigations on the tensile mechanical behavior of marbles containing dynamic damage. International Journal of Mining Science and Technology, 2022, 32(1): 89-102.

Zhao, X., Huang, B., Chen, B., et al. Experimental investigation of the effect of evenly distributed pore pressure on rock damage. Lithosphere, 2022, 2022: 1759146.

Zhao, Y., Bi, J., Zhou, X. Quantitative analysis of rockburst in the surrounding rock masses around deep tunnels. Engineering Geology, 2020, 273: 105669.

Zhou, S., Zhuang, X., Rabczuk, T. A phase-field modeling approach of fracture propagation in poroelastic media. Engineering Geology, 2018, 240: 189-203.

Zhou, X., Shen, F., Berto, F. Experimental study on triaxial creep behavior of red sandstone under different pore pressures based on ultrasonic measurement. Fatigue & Fracture of Engineering Materials & Structures, 2022, 45(8): 2388-2402.

Zhu, H., Liu, Q., Wong, G., et al. A pressure and temperature preservation system for gas-hydrate-bearing sediments sampler. Petroleum Science and Technology, 2013, 31(6): 652-662.

Zhu, W., Wei, C., Liu, J., et al. A model of coal-gas interaction under variable temperatures. International Journal of Coal Geology. 2011, 86(2-3): 213-221.